Rotational-State-Dependent Dispersion of Molecules by Pulsed Optical Standing Waves

Xing Nan Sun,[1,2] Lee Yeong Kim,[3] Bum Suk Zhao (조범석),[2,3,*] and Doo Soo Chung[1,*]
[1]Department of Chemistry, Seoul National University, Seoul, Korea
[2]Department of Chemistry, Ulsan National Institute of Science and Technology, Ulsan, Korea
[3]Department of Physics, Ulsan National Institute of Science and Technology, Ulsan, Korea
(Received 14 July 2015; published 24 November 2015)

We report on the rotational-state-dependent, transverse acceleration of CS_2 molecules affected by pulsed optical standing waves. The steep gradient of the standing wave potential imparts far stronger dipole forces on the molecules than propagating pulses do. Moreover, large changes in the transverse velocities (i.e., up to 80 m/s) obtained with the standing waves are well reproduced in numerical simulations using the effective polarizability that depends on the molecular rotational states. Our analysis based on the rotational-state-dependent effective polarizability can therefore serve as a basis for developing a new technique of state selection for both polar and nonpolar molecules.

DOI: 10.1103/PhysRevLett.115.223001 PACS numbers: 37.10.Vz, 33.15.-e, 33.80.-b, 37.20.+j

During the last two decades, optical manipulation of molecules has been an important subject in many experimental and theoretical studies. A nonresonant laser field exerts a dipole force on molecules proportional to the molecular polarizability. Propagating nonresonant laser fields have been used to control the angular, transverse, and longitudinal motions of molecules. Strong laser pulses have been used to align molecules [1,2]. A combination with an electrostatic field produces an orientation of polar molecules [3–8]. Focusing a molecular beam [9] and separating a molecular mixture beam [10] were proposed, and a molecule lens [11–13] and a molecule prism [14] have been realized. It was also suggested that molecules could be decelerated using a nonresonant laser field [15,16]. Coupling between the angular and the translational motions enabled the adjustments of the deceleration by aligning the molecules with the laser field [17,18]. In addition, efficient control of molecular deflection by preshaping the angular distribution was discussed [19,20].

On the other hand, the standing wave potential, formed by two counterpropagating lasers, has been employed to control the forward velocity of molecules. An atom and molecule mirror made of a pulsed standing wave was suggested [21]. An accelerator [22] and a decelerator [23] for atoms and molecules using pulsed traveling standing waves with increasing and decreasing velocities, respectively, were discussed. Furthermore, the possibility of slowing down and bunching molecules by means of a traveling potential with a constant velocity was studied [24]. These theoretical studies were followed by experimental realizations. A pulsed standing wave changed the velocity distribution of hydrogen molecules by 200 m/s [25]. Traveling potentials with constant velocities were used to decrease the velocity of NO molecules [26] and to prepare stationary benzene molecules [27]. Recently, the velocity of metastable argon atoms initially trapped in a magneto-optical trap was accelerated by an accelerating periodic potential [28].

The angular motions of molecules determine their effective polarizabilities, which in turn affect their translational motions in a manner dependent on the rotational states. Thus the interaction between molecules and laser fields was recognized to be rotational-state-dependent [1,2,4,9,10,19,20,29–31], and the possibility of separating quantum states with laser fields was discussed in theoretical studies [10,19,20,29–32]. However, almost all the experimental results [2,11–14,17,26,27] were analyzed using a single polarizability value averaged over all quantum states.

Here we report on the transverse dispersion of a CS_2 molecular beam by pulsed optical standing waves and its interpretation in terms of the rotational-state-dependent molecular polarizability. The velocity spread of the dispersed molecules is about 160 m/s, which is too large to be accounted for solely by using the average polarizability. For this reason, we use the rotational-state-dependent polarizability to simulate the velocity spreads, which are in excellent agreement with the experimental results. In this way, we demonstrate the dependence of the dipole force on the rotational states, and show its importance in understanding molecular transverse motions affected by optical standing waves. Our report therefore serves as a cornerstone for developing a new state-selection technique that is potentially applicable to both polar and nonpolar molecules. The control over the molecular transverse motion is complementary to the deceleration and acceleration of molecules [25–28].

A schematic of the experimental setup is shown in Fig. 1. The apparatus operates at 10 Hz. We define the y and z axes as the vertical and the molecular beam directions, respectively. The infrared laser (IR1) propagates parallel to the positive x axis. The coordinate origin is at the IR1 focus, which overlaps with the IR2 focus. The molecular beam is

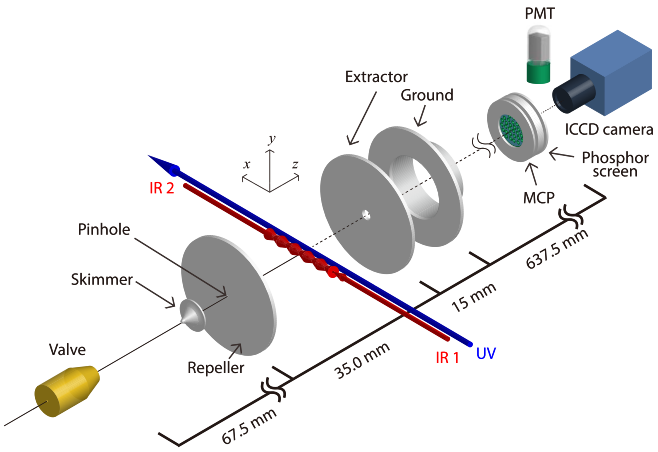

FIG. 1 (color online). Schematics of the experimental setup.

formed by seeding 0.3 vol% CS_2 vapor in Ar gas and expanding the mixture, held at a pressure of 2 atm, through a pulsed valve of a nozzle into a vacuum chamber. With similar source conditions, the rotational temperature T was estimated to be 35 K in the previous report [17]. After passing through a skimmer, the molecular beam enters a second chamber at 1×10^{-7} Torr. The molecular beam is then collimated by a pinhole. At 8.5 cm downstream from the nozzle, the molecular beam is crossed by a pulsed standing wave potential.

The pulsed standing wave is created by overlapping two counterpropagating pulses (IR1 and IR2) with the same peak intensity I_0 at the center of the second chamber. Their pulse width and wavelength are $\tau = 12.5$ ns (FWHM) and $\lambda = 1064$ nm, respectively. The two pulses are formed by splitting a single pulse from an injection-seeded Nd:YAG laser. After splitting, the energy and polarization of the two pulses are adjusted by two sets of a zero-order half-wave plate and a Glan-Laser polarizer, respectively. Then the two pulses, which are linearly polarized along the y axis, are focused by two lenses with focal lengths of 20 cm into the second chamber. The waist radius ω_0 of the pulses is 21 μm.

After a delay of 30 ns, the molecular beam, which has interacted with the pulsed standing wave potential, intersects with an lineraly polarized ultraviolet (UV) probe laser pulse which is a third-harmonic of another Nd:YAG laser with $\tau = 7.1$ ns and $\lambda = 355$ nm. The lens in front of the second chamber also focuses the UV pulse. Considering the delay of 30 ns, the UV laser focus is also spatially shifted along the z axis to ionize only the dispersed molecules through multiphoton ionization processes.

The dispersed and subsequently ionized molecules are accelerated and focused by an electrostatic lens system onto a microchannel plate (MCP) after flying 67 cm through a time-of-flight (TOF) tube. Three electrodes, a repeller (900 V), an extractor (600 V), and a ground provide the velocity map imaging condition [33]. In this way, the transverse velocity of an ion is measured from the ratio between its position at the detector and the TOF. The ion signals are converted into luminescence by an MCP and a phosphor screen, which is simultaneously detected by a photomultiplier tube (PMT) and an intensified charge-coupled device (ICCD) camera.

Figure 2(a) shows a velocity map image of CS_2 molecular ions without IR1 or IR2. When only IR1 of low intensity is applied to the molecular beam, it hardly affects the molecular velocity distribution. Figure 2(b) shows an ion image with IR1 of $I_0 = 4.9 \times 10^{10}$ W/cm^2, almost identical to Fig. 2(a) obtained without any IR pulses. The intensity of the UV pulse is 0.8×10^{10} W/cm^2. However, when a pulsed standing wave is formed by IR1 and IR2 with their intensities set to 4.9×10^{10} W/cm^2 each, a drastic change takes place, as shown in Fig. 2(c). $|v_x|$ increases to about 60 m/s, whereas v_y is affected little.

The rotational-state-dependent molecular polarizability is the key to understanding the structures shown in the velocity distribution in Fig. 2(c). The interaction potential between the standing wave field with wavelength λ and waist radius ω_0 and a molecule with an effective molecular polarizability α_{eff} at time t is given by

$$U(x,y,z,t) = -2\alpha_{\text{eff}}\eta_0 I_0 \exp[-2(y^2+z^2)/\omega_0^2] \times \exp[-4(\ln 2)t^2/\tau^2]\cos^2(2\pi x/\lambda), \quad (1)$$

with the vacuum impedance η_0. The first and second exponential terms represent the spatial and temporal profiles, respectively, whereas the $\cos^2(2\pi x/\lambda)$ term corresponds to its periodic variation along the x axis. The force on the molecule $\mathbf{F}(x,y,z,t) = -\nabla U(x,y,z,t)$ along the x and y axes is characterized by the inverse of λ and ω_0, respectively. Therefore, the maximum accelerations along the x and y axes differ by a factor of 20.

A linear molecule such as CS_2 has an anisotropic polarizability, whose components parallel and perpendicular to

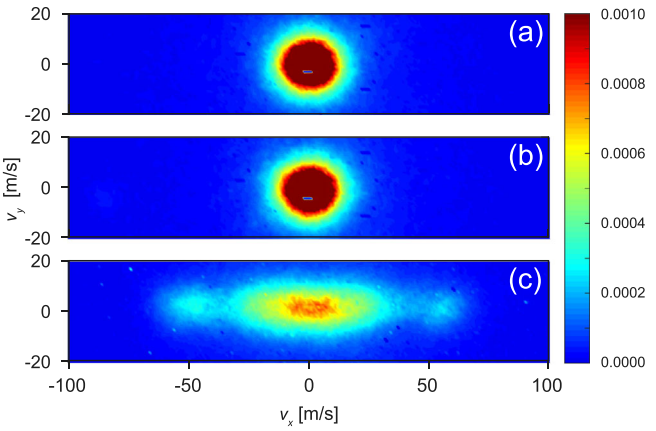

FIG. 2 (color online). The velocity map ion images of CS_2 molecules (a) without any IR laser, (b) with IR1 of $I_0 = 4.9 \times 10^{10}$ W/cm^2, and (c) with the pulsed optical standing wave made of IR1 and IR2 of $I_0 = 4.9 \times 10^{10}$ W/cm^2. The color bar in the image denotes the fraction of the molecules.

the molecular axis are $\alpha_\parallel$ and $\alpha_\perp$, respectively. When a linear molecule is oriented at a polar angle θ with respect to the laser polarization axis, the effective polarizability is given by $\alpha_{\rm eff} = (\alpha_\parallel - \alpha_\perp)\overline{\cos^2\theta} + \alpha_\perp$. For a rotational state $|J, M\rangle$,

$$\overline{\cos^2\theta} = \langle J, M|\cos^2\theta|J, M\rangle = \frac{1}{3} + \frac{2}{3}\frac{J(J+1) - 3M^2}{(2J+3)(2J-1)}. \quad (2)$$

Therefore, the effective polarizability varies with J and M, the quantum numbers associated with the angular momentum and its projection on the laser polarization axis, respectively. At a rotational temperature of $T = 35$ K, the value of $\alpha_{\rm eff}(J, M)$ for CS_2 ($\alpha_\parallel = 16.8\times 10^{-40}$ C m^2 V^{-1} and $\alpha_\perp = 6.2 \times 10^{-40}$ C m^2 V^{-1} [34]) varies from 6.2 to 12.6×10^{-40} C m^2 V^{-1} with an average of 9.7×10^{-40} C m^2 V^{-1}. On the other hand, at very low rotational temperatures, a few states of low J are populated, whose effective polarizabilities are rather discrete. For example, $\alpha_{\rm eff}(2, M) = 11.8$, 10.7, and 7.7×10^{-40} C m^2 V^{-1} for $|M| = 0$, 1, and 2, respectively. Thus, each state is affected quite differently, which can, in principle, be exploited to separate the different rotational states.

Figure 3 shows how the rotational-state-dependent polarizability contributes to the velocity distribution of Fig. 2(c). Considering the negligible effect of the standing wave on v_y as shown in Fig. 2, instead of the two-dimensional velocity distribution function for molecules dispersed by the standing wave, $g(v_x, v_y)$, we use its profile $h(v_x)$ along the v_x axis, in other words, the binning of $g(v_x, v_y)$ along the v_y axis. The velocity change that results from the dipole force of $\mathbf{F}$ on a molecule of mass m is given by

$$\Delta v_i = \int \frac{1}{m} F_i(x, y, z, t)dt \quad (i = x, y, z,), \quad (3)$$

which is solved numerically. Since $U(x, y, z, t)$ is proportional to $\alpha_{\rm eff}$, which is a function of J and M, the force on the molecule depends on the molecular rotational state, and so does the velocity change. Here, we assume that the CS_2 molecules are not aligned by the laser field, since the alignment effect of CS_2 molecules is negligible at field intensities below 1.0×10^{11} W/cm^2 [35]. Trajectory calculations of 9×10^6 molecules yield the velocity distribution $g(v_x, v_y)$. The initial velocity (v_{0x}, v_{0y}, v_{0z}), initial position (x_0, y_0, z_0), and rotational state of an individual molecule are sampled by the Monte Carlo method. The initial transverse velocity distribution is approximated by a two-dimensional Gaussian function with FWHMs of $\Delta v_x^{\rm init} = 7.2$ and $\Delta v_y^{\rm init} = 3.4$ m/s, which are given by line-of-sight arguments [11]. The asymmetric spreads result from the ionization volume being elongated along the x axis. A Gaussian distribution with the most probable velocity $v_{\rm mp}$ of 560 m/s [36] and FWHM of 56 m/s is used as a probability function for v_{0z}. Here, we assume that

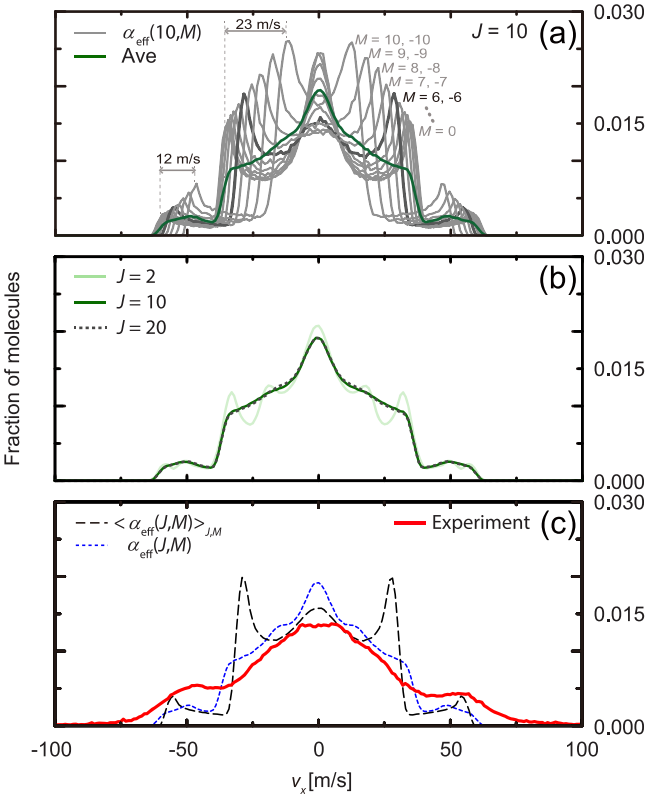

FIG. 3 (color online). (a) Simulated velocity profiles for 21 rotational states of $J = 10$ (gray lines) and their average (dark green solid line). (b) Similar summation profiles for $J = 2$, 10, and 20. (c) Comparison of the velocity profile of Fig. 2(c) (red line) with those calculated by using state-dependent [$\alpha_{\rm eff}(J, M)$; blue dotted line] and state-independent polarizabilities [$\langle\alpha_{\rm eff}(J, M)\rangle_{J,M}$; black dashed line].

the FWHM is 10% of the most probable velocity [25,37]. x_0 and y_0 are chosen randomly from a 600×3 μm rectangle. The range of the distribution is approximate to the ionization range. We ignore the beam divergence and consider the multiphoton ionization process involving three photons.

On the other hand, z_0 is determined from v_{0z} such that the individual molecule arrives at the plane $z = v_{\rm mp}t_{\rm delay}$ at $t = t_{\rm delay}$. Therefore, $z_0 = v_{\rm mp}t_{\rm delay} - v_{0z}t_{\rm simul}$, where $t_{\rm delay}$ and $t_{\rm simul}$ are the delay between the two IRs and the probe laser beam and the total simulation time, respectively. The molecule occupies a certain $|J, M\rangle$ state with a probability P_J of $e^{-BJ(J+1)/kT}/q_{\rm r}$, where B, k, and $q_{\rm r}$ are the rotational constant of the molecule, Boltzmann constant, and rotational partition function, respectively. J is restricted to even numbers because of the zero nuclear spin of ^{32}S [38]. The trajectory calculation includes a thermal distribution of molecules over rotational states at $T = 35$ K, which was estimated in the previous Letter [17]. It is worth noting that a temperature change of ± 10 K hardly affects the simulation results. Here, we use $\omega_0 = 23.5$ μm and $\tau = 10$ ns, which are within the error ranges of the measured values of $\omega_0 = 21.5 \pm 2$ μm and $\tau = 12.5 \pm 2$ ns, respectively.

In Fig. 3(a), 21 profiles of $h(v_x; J = 10, M)$ are drawn in gray lines, assuming that all the molecules occupy each $|J = 10, M\rangle$ state. Since $h(v_x; J = 10, M) = h(v_x; J = 10, -M)$, they are overlapped in Fig. 3(a) and the total number of the profiles is 21. In each profile, there are strong rainbowlike singularities associated with the existence of the maxima (minima) in the deflecting standing wave [39], whose positions move outward as $|M|$ decreases—i.e., as $\alpha_{\rm eff}$ increases. As $\alpha_{\rm eff}(10, |M|)$ ranges from 6.7 ($|M| = 10$) to 11.5 ($|M| = 0$) $\times 10^{-40}$ C m^2 V^{-1}, the positions of the inner and the outer singularities span from ± 12 to ± 35 and from ± 46 to ± 58 m/s, respectively. The congestions of the profiles near ± 35 and ± 58 m/s manifest the unimodal rainbow feature in the distribution of $\alpha_{\rm eff}$, which was predicted by Gershnabel and Averbukh [20]. The green solid line in Fig. 3(a) represents the average of the 21 profiles $[1/(2 \times 10 + 1)] \sum_{M=-10}^{10} h(v_x; J = 10, M)$, which is the convolution of the two types of rainbowlike singularities. Note that the inner singularities are smeared out owing to the large distribution of their positions. In contrast, the spread of the positions of the outer singularity forms two broad small peaks in the green profile.

Figure 3(b) shows $[1/(2J + 1)] \sum_{M=-J}^{J} h(v_x; J, M)$ for $J = 2$, 10, and 20. These three J states are selected because, at $T = 35$ K, the population of the rotational energy levels has its maximum at $J = 10$, and is close to half of the maximum at $J = 2$ and 20. Note that the profile for $J = 2$ is more structured than the other two. Furthermore, the two profiles for $J = 10$ and 20 are almost identical.

The blue dotted profile in Fig. 3(c) is $\sum_{J,M} P_J h(v_x; J, M)$ obtained by considering the rotational states up to $J = 98$. The inner rainbowlike peaks of the profile are smeared out, though the outer ones leave small peaks, as in Fig. 3(b). These features also appear in the red line in Fig. 3(c), which is the profile of the measured velocity distribution in Fig. 2(c). The black dashed line in Fig. 3(c) depicts $h[v_x; \alpha_{\rm eff}(T)]$, assuming that all the molecules possess the same polarizability $\alpha_{\rm eff}(T) = \langle \alpha_{\rm eff}(J, M) \rangle_{J,M}$. This profile is almost identical to the thick gray profile in Fig. 3(a)—i.e., the profile for $|J = 10, M = \pm 6\rangle$ with $\alpha_{\rm eff} = 9.8 \times 10^{-40}$ C m^2 V^{-1}. It shows distinctive inner singularities, which clearly disagrees with the experimental result. For these reasons, the state-dependent effective polarizability can be identified as the crucial contribution to the final velocity distribution.

The velocity distribution of the dispersed molecules in a rotational state varies as the intensity increases. In addition to the increase in the distribution width, the shape changes with the laser intensity. Figure 4 shows ion images and their velocity profiles (red lines) at $I_0 = (a)$ 1.0, (b) 4.9, and (c) 9.8×10^{10} W/cm^2, each of which is compared with two simulated profiles using the state-dependent polarizability $\alpha_{\rm eff}(J, M)$ (blue dotted lines) and the state-averaged polarizability $\langle \alpha_{\rm eff}(J, M) \rangle_{J,M}$ (black dashed lines). As I_0 increases, the velocity of molecules becomes distributed across a wider range (up to about ± 80 m/s), and the structure of the distribution varies. The initial velocity profile ($\times 1/3$) is shown in Fig. 4(a) with a gray line, for comparison. The full series of the ion images and the velocity profiles are shown in Figs. S1 and S2, respectively, in the Supplemental Material [40]. At $I_0 = 1.0 \times 10^{10}$ W/cm^2, the experimental profile exhibits a trapezoidal shape. A couple of side peaks appear at $I_0 = 2.0 \times 10^{10}$ W/cm^2. The side peaks move outward and become less distinctive as I_0 increses up to 5.9×10^{10} W/cm^2, but these peaks disappear when I_0 is further increased. As disccused above, the side peaks are associated with the relatively narrow spread of outer rainbowlike sigularities, as in Fig. 3(a). Therefore, the broadening of the spread, due to the increase of I_0, makes the side peaks become less distinguished, and they ultimately disappear.

This variation is well reproduced in the blue simulated profiles using the state-dependent polarizability. On the other hand, similar to the comparison in Fig. 3(c), the black profiles simulated using the state-averaged polarizability severely disagree with the red experimental profiles at the parts related to the inner rainbowlike sigularities. The inner singularities are very sharp in the black simulated profiles, but are smeared out in the red experimental and blue simulated profiles. These comparisons corroborate the fact that the state-dependent effective polarizability should be considered in analyzing the transverse velocity change that results from a pulsed standing wave potential.

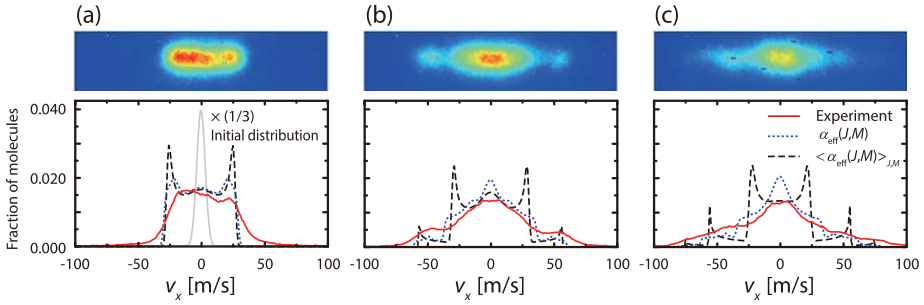

FIG. 4 (color online). The three velocity map ion images of CS_2 molecules with the standing wave of $I_0 = (a)$ 1.0×10^{10}, (b) 4.9×10^{10}, and (c) 9.8×10^{10} W/cm^2 and their profiles along the v_x axis. The exprimental profiles (red lines) are compared with the simulated ones by using $\alpha_{\rm eff}(J, M)$ (blue dotted lines) and $\langle \alpha_{\rm eff}(J, M) \rangle_{J,M}$ (black dashed lines), as in Fig. 3(c).

Together with other state-of-the-art techniques, such as a pulsed supersonic expansion source [41] and optical standing waves of a tunable velocity [26,28], the state-dependent dispersion is expected to enable state selection of nonpolar molecules. The relative velocity of molecules to the moving standing wave can be made such that only the state of the highest α_{eff} is trapped in the standing wave potential. In this way, the trapped state can be separated from other untrapped states. The detailed scheme of the state selection is described in the Supplemental Material [40]. This new method will nicely complement the techniques for the state selection of polar molecules [42,43]. Especially, this optical technique can be exploited to separate and analyze mixtures of nonpolar conformers, isotopes of homonuclear diatomic molecules, or their spin isomers.

In conclusion, we observed the rotational-state-dependent dispersion of CS_2 molecules by optical standing waves. Simulations using the state-dependent polarizabilities provided better agreement with the experimental observations as compared with simulations based on the average (state-independent) polarizability. This paves the way for selecting a specific state of nonpolar molecules.

This work was supported by the Basic Science Research Program through the National Research Foundation of Korea funded by the Ministry of Education, Science and Technology (NRF-2013R1A1A2059715 and NRF-2012R1A1A1041789). B. S. Z. acknowledges support from the T. J. Park Science Fellowship.

X. N. S. and L. Y. K. contributed equally to this work.

*Corresponding authors.
zhao@unist.ac.kr

[1] B. Friedrich and D. Herschbach, Phys. Rev. Lett. **74**, 4623 (1995).
[2] H. Stapelfeldt and T. Seideman, Rev. Mod. Phys. **75**, 543 (2003).
[3] B. Friedrich and D. Herschbach, J. Chem. Phys. **111**, 6157 (1999).
[4] B. Friedrich and D. Herschbach, J. Phys. Chem. A **103**, 10280 (1999).
[5] L. Cai, J. Marango, and B. Friedrich, Phys. Rev. Lett. **86**, 775 (2001).
[6] H. Sakai, S. Minemoto, H. Nanjo, H. Tanji, and T. Suzuki, Phys. Rev. Lett. **90**, 083001 (2003).
[7] M. Härtelt and B. Friedrich, J. Chem. Phys. **128**, 224313 (2008).
[8] J. H. Nielsen, H. Stapelfeldt, J. Küpper, B. Friedrich, J. J. Omiste, and R. González-Férez, Phys. Rev. Lett. **108**, 193001 (2012).
[9] T. Seideman, J. Chem. Phys. **106**, 2881 (1997).
[10] T. Seideman, J. Chem. Phys. **107**, 10420 (1997).
[11] H. Stapelfeldt, H. Sakai, E. Constant, and P. B. Corkum, Phys. Rev. Lett. **79**, 2787 (1997).
[12] B. S. Zhao *et al.*, Phys. Rev. Lett. **85**, 2705 (2000).
[13] H. S. Chung, B. S. Zhao, S. H. Lee, S. Hwang, K. Cho, S.-H. Shim, S.-M. Lim, W. K. Kang, and D. S. Chung, J. Chem. Phys. **114**, 8293 (2001).
[14] B. S. Zhao, S. H. Lee, H. S. Chung, S. Hwang, W. K. Kang, B. Friedrich, and D. S. Chung, J. Chem. Phys. **119**, 8905 (2003).
[15] B. Friedrich, Phys. Rev. A **61**, 025403 (2000).
[16] R. Fulton, A. I. Bishop, and P. F. Barker, Phys. Rev. Lett. **93**, 243004 (2004).
[17] S. M. Purcell and P. F. Barker, Phys. Rev. Lett. **103**, 153001 (2009).
[18] S. M. Purcell and P. F. Barker, Phys. Rev. A **82**, 033433 (2010).
[19] E. Gershnabel and I. S. Averbukh, Phys. Rev. Lett. **104**, 153001 (2010).
[20] E. Gershnabel and I. S. Averbukh, Phys. Rev. A **82**, 033401 (2010).
[21] P. Ryytty and M. Kaivola, Phys. Rev. Lett. **84**, 5074 (2000).
[22] P. F. Barker and M. N. Shneider, Phys. Rev. A **64**, 033408 (2001).
[23] P. F. Barker and M. N. Shneider, Phys. Rev. A **66**, 065402 (2002).
[24] G. Dong, W. Lu, and P. F. Barker, Phys. Rev. A **69**, 013409 (2004).
[25] J. Ramirez-Serrano, K. E. Strecker, and D. W. Chandler, Phys. Chem. Chem. Phys. **8**, 2985 (2006).
[26] R. Fulton, A. I. Bishop, M. N. Shneider, and P. F. Barker, Nat. Phys. **2**, 465 (2006).
[27] A. I. Bishop, L. Wang, and P. F. Barker, New J. Phys. **12**, 073028 (2010).
[28] C. Maher-McWilliams, P. Douglas, and P. F. Barker, Nat. Photonics **6**, 386 (2012).
[29] E. Gershnabel and I. S. Averbukh, J. Chem. Phys. **134**, 054304 (2011).
[30] E. Gershnabel and I. S. Averbukh, J. Chem. Phys. **135**, 084307 (2011).
[31] E. Gershnabel, M. Shapiro, and I. S. Averbukh, J. Chem. Phys. **135**, 194310 (2011).
[32] S. Fleischer, I. S. Averbukh, and Y. Prior, Phys. Rev. Lett. **99**, 093002 (2007).
[33] A. T. J. B. Eppink and D. H. Parker, Rev. Sci. Instrum. **68**, 3477 (1997).
[34] J. O. Hirschfelder, C. F. Curtiss, and R. B. Bird, *Molecular Theory of Gases and Liquids* (Wiley, New York, 1954).
[35] R. Velotta, N. Hay, M. B. Mason, M. Castillejo, and J. P. Marangos, Phys. Rev. Lett. **87**, 183901 (2001).
[36] G. Scoles, D. Bassi, U. Buck, and U. Valbusa, *Atomic and Molecular Beam Methods* (Oxford University Press, New York, 1988).
[37] S. M. Purcell, Ph.D. thesis, University College London, 2010.
[38] R. Torres, R. de Nalda, and J. P. Marangos, Phys. Rev. A **72**, 023420 (2005).
[39] P. Atkins and J. de Paula, *Atkins' Physical Chemistry*, 9th ed (Oxford University Press, New York, 2014).
[40] See Supplemental Material at http://link.aps.org/supplemental/10.1103/PhysRevLett.115.223001 for the full series of the ion images, the velocity profiles, and the detailed scheme of the state selection.
[41] M. Hillenkamp, S. Keinan, and U. Even, J. Chem. Phys. **118**, 8699 (2003).
[42] S. Y. T. van de Meerakker, H. L. Bethlem, and G. Meijer, Nat. Phys. **4**, 595 (2008).
[43] F. Filsinger, J. Küpper, G. Meijer, J. L. Hansen, J. Maurer, J. H. Nielsen, L. Holmegaard, and H. Stapelfeldt, Angew. Chem., Int. Ed. Engl. **48**, 6900 (2009).